Progress In Electromagnetics Research C, Vol. 128, 155–168, 2023

A Flexible CPW 2-Port Dual Notched-Band UWB-MIMO Antenna for Wearable IoT Applications

Xin You, Cheng-Zhu Du*, and Zhi-Peng Yang

Abstract—In this paper, a flexible 2-port MIMO antenna with dual band-notched properties is designed and built for wireless body area network applications. The antenna's performance in its flat and bent states is measured using liquid crystal polymer as a substrate. Two UWB slot antenna components are arranged in parallel with linked ground. Furthermore, to achieve high port isolation, a decoupling device in the form of a fence is positioned between two antenna units. The measured operating bandwidth can reach 3.0–15.7 GHz, with blocking bands of 5.0–6.5 and 7.0–7.9 GHz. Port isolation (S_{21}) is better than 20 dB. This antenna has fine radiation properties, high isolation, and flexibility, according to the bending and flat antenna tests. It has a promising future for wearable Internet of Things applications.

1. INTRODUCTION

With the development of communication technology, high capacity, multiple connectivity, and high speed have become urgent need. Multiple-input multiple-output (MIMO) technology and ultra-wideband (UWB) will considerably enhance data transmission efficiency, suppress the multipath effect, and enhance communication quality and capacity [1–3]. However, there is interference from narrowband in UWB, such as WLAN (5.15–5.825 GHz) and X downlink band (7.25–7.75 GHz). It is essential to design UWB MIMO antennas with strong isolation and narrowband interference filtering [4]. As the UWB MIMO antenna is printed on a flexible substrate, it is suitable for the wearable Internet of Things (IoT) and wireless personal local area network (WBAN) applications.

Numerous UWB-MIMO antennas have been designed [5–14]. In [5], a fractal notched-band UWB-MIMO antenna used FR4 as substrate is designed, operating between 2 and 14 GHz with high isolation ($S_{12} < -30$ dB) in WBAN systems. According to [6], a UWB MIMO antenna covering the range of 3.0–10.7 GHz is built with four notched bands. A UWB-MIMO antenna having four elements with dual-band notch characteristics is described in [7], and the isolation is higher than 20 dB at all operational frequencies. All of the above MIMO antennas use rigid dielectric plates and do not work in bending conditions.

Some flexible MIMO antennas are designed for the WBAN field and IoT applications [8–13]. Reference [8] suggests a flexible MIMO antenna for a flexible IoT wireless system, achieving high isolation (S_{12-23} dB) and wide bandwidth (3.2–13 GHz). Ref. [9] proposes a 2.4 GHz and UWB-based toroidal four-port MIMO antenna with Silicone rubber as the dielectric substrate for wearable applications. A paper-based MIMO antenna with a 2.22–3.85 GHz bandwidth range is suggested in [10]. Ref. [11] demonstrates a wearable, lightweight, dual-element UWB MIMO antenna built from denim. According to [12], a planar UWB MIMO antenna is built to be worn on the arm for the use in WBAN applications. In [13], based on a liquid crystal polymer (LCP) substrate, a co-planar waveguide (CPW)-fed flexible

Received 7 November 2022, Accepted 20 December 2022, Scheduled 9 January 2023

* Corresponding author: Cheng-Zhu Du (duchengzhu@163.com).

The authors are with the College of Electronics and Information Engineering, Shanghai University of Electric Power, Shanghai 200090, China.

band-notched UWB MIMO antenna is designed. The antenna's impedance bandwidth is 890 MHz (2.4–11.3 GHz) with 23 dB port isolation.

In this study, a flexible small UWB-MIMO antenna with connected ground is designed. The CPW-fed antenna is based on an ultra-thin LCP substrate. The UWB slot antenna element is composed of a circular radiating patch. The two antenna elements are placed in parallel with connected ground. In order to improve isolation, three fence-like isolation branches are placed between the antenna units. The antenna's size is 56 mm × 30 mm × 0.1 mm. The measured antenna has ultra-wide band of 3.0–15.7 GHz and two notched bands of 5.0–6.5 and 7.0–7.9 GHz. The measured port isolation (S_{21}) of the antenna is all less than −20 dB. In addition, the performance of the flexible UWB-MIMO antenna under different bending cases is analyzed.

The ultrathin MIMO antenna is a good candidate for wearable IoT applications as follows: (1) the bandwidth can reach 3.0–15.7 GHz, with dual notched bands of 5.0–6.5 and 7.0–7.9 GHz; (2) CPW feed facilitates the antenna integration into circuits; and (3) the flexibility of LCP material.

2. DESIGN AND ANALYSIS OF ANTENNAS

2.1. Antenna Structure

In Figure 1(a), the proposed antenna's planar construction is depicted. It is fed by a CPW and printed on a 0.1 mm LCP substrate (2.9 relative dielectric constant and 0.002 loss tangent). The two antenna elements are positioned in parallel with connected ground. The design method of single element antenna is the same as [14]. The fence-shaped decoupling branches are placed between the antenna elements to attain high port isolation. The dimensions are 56 mm × 30 mm × 0.1 mm. The antenna element is designed as a circular patch, and two arc-shaped corners are cut off on the ground plane for good impedance matching. To create two notched bands of the WLAN signal and X signal, two C-shaped slots are engraved onto the ground plane. The slot's length is determined as follows:

$$L = \frac{C}{4f_c \times \sqrt{\varepsilon_{eff}}} \tag{1}$$

where C stands for the speed of light, f_c the notch center frequency, and ε_{eff} the dielectric constant's effective value. A photo of the fabricated flexible MIMO antenna is presented in Figure 1(b). The size parameters of antenna are listed in Table 1.

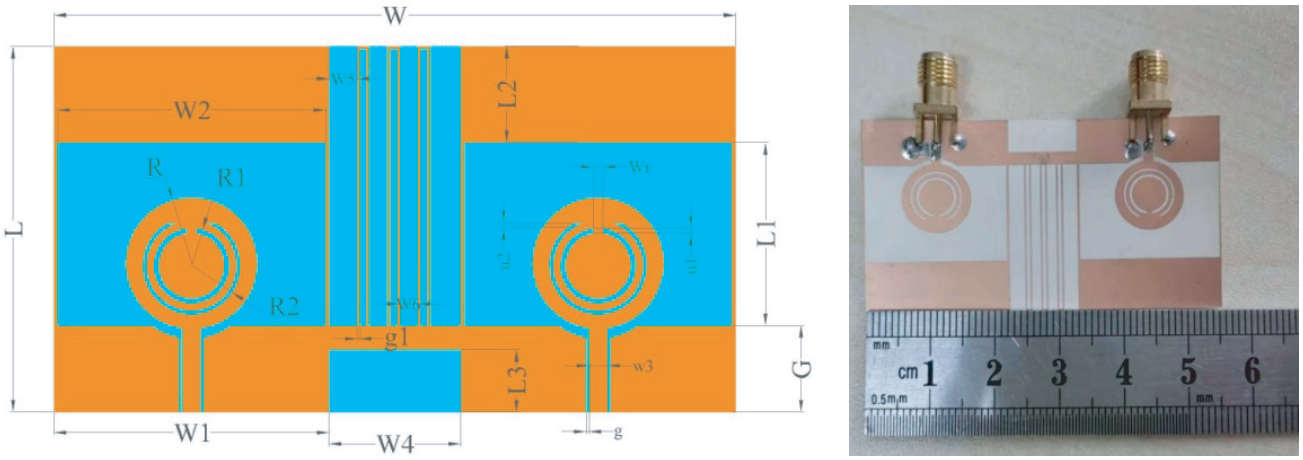

(a) (b)

Figure 1. The construction of the antenna. (a) Geometrical details. (b) Fabricated antenna.

Table 1. Size parameters of antenna (mm).

parameter	value	parameter	value
W	56	L	30
$W1$	22.6	$L1$	15
$W2$	22	$L2$	7.9
$W3$	1.5	$L3$	5.1
$W4$	10.8	G	7.1
$W5$	2.3	g	0.25
$W6$	1.5	$g1$	0.2
Wr	0.8	R	5.4
$R1$	3.1	$R2$	4
$u1$	0.4	$u2$	0.3

2.2. Design Process of the Flexible MIMO Antenna

Figure 2 shows the antenna design process. In Figure 3 and Figure 4, various antennas' simulated S-parameters are displayed.

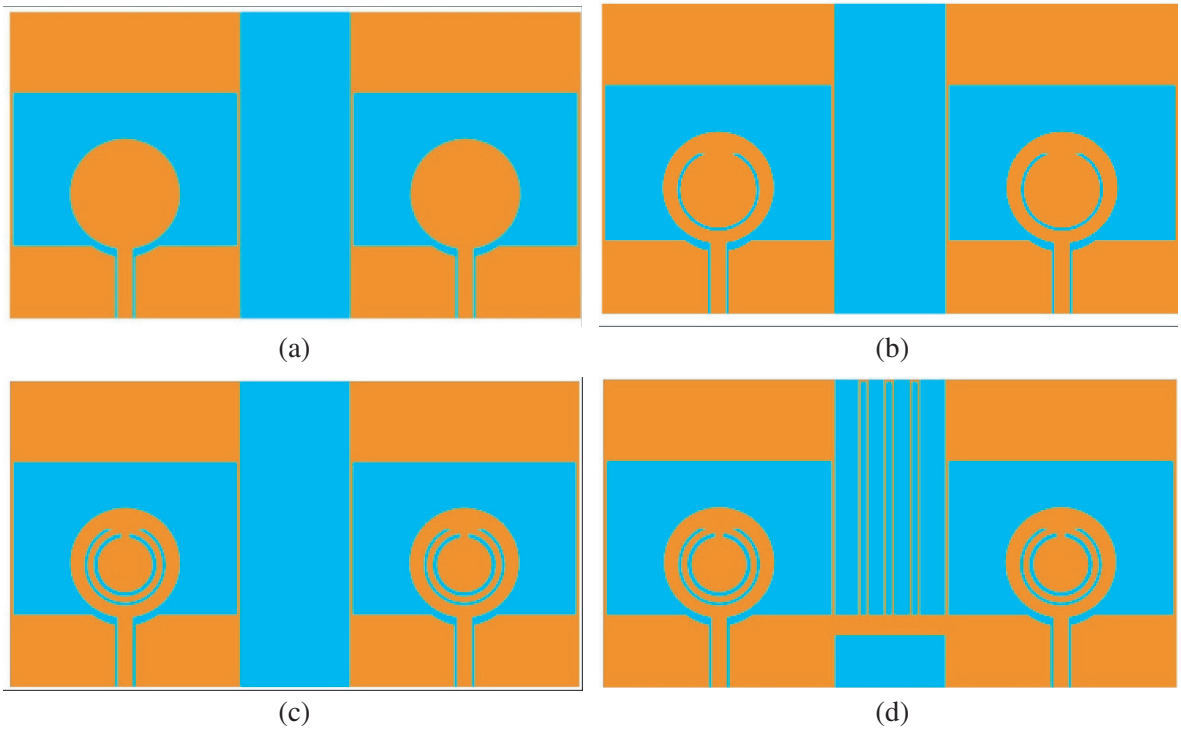

Figure 2. The procedure for the design of the potential antenna. (a) Ant I. (b) Ant II. (c) Ant III. (d) Ant IV.

Ant I is the first step of the antenna design process. Two antenna units are placed parallelly with a certain distance. The antenna impedance bandwidth is improved by cutting corner on the ground. The antenna impedance bandwidth ($S_{11} < -10\,\text{dB}$) is 3.9–11.45 GHz, and the isolation is all below $-14.5\,\text{dB}$.

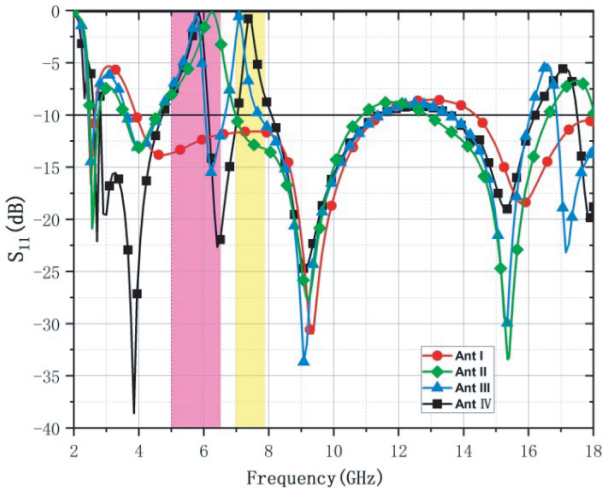

Figure 3. S_{11} of four different antennas.

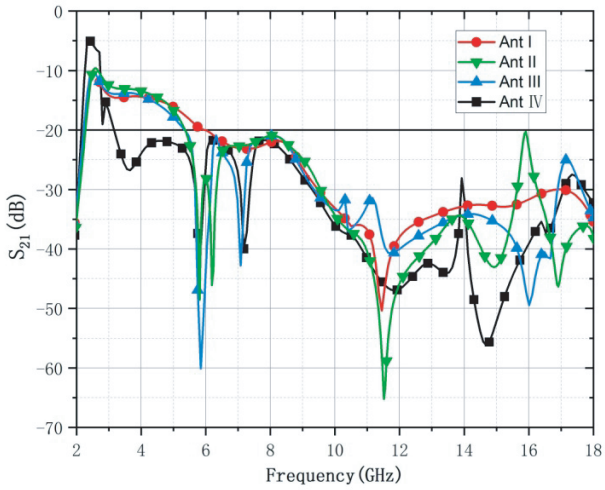

Figure 4. S_{21} of four different antennas.

Ant II is the second step of the antenna design process. The target notched-band is generated by adding a slot on the antenna patch. A lengthy C-slot is etched onto Ant I to create Ant II. When the long C-slot is engraved, it can be seen from Figure 3 that a notched band (4.5–6.5 GHz) is generated. Ant III is the third step of the antenna design process. Ant III is designed by etching two short C-slots on Ant II. According to the simulation of Ant III, $S_{11} < -10$ dB is now from 3.8–11.4 GHz, with the exception of two rejected bands (4.8–6.1 GHz and 6.8–7.7 GHz), which effectively reduce interferences in the WLAN band and X band; however, the isolation is still below −14 dB.

Finally, to attain high port isolation further, the fence-shaped decoupling branches are placed among the antenna elements and connected to the ground, namely Ant IV. According to the simulation of Ant IV, in the impedance bandwidths of 3.1–1.4 GHz, the isolation of Ant IV is better than 20 dB.

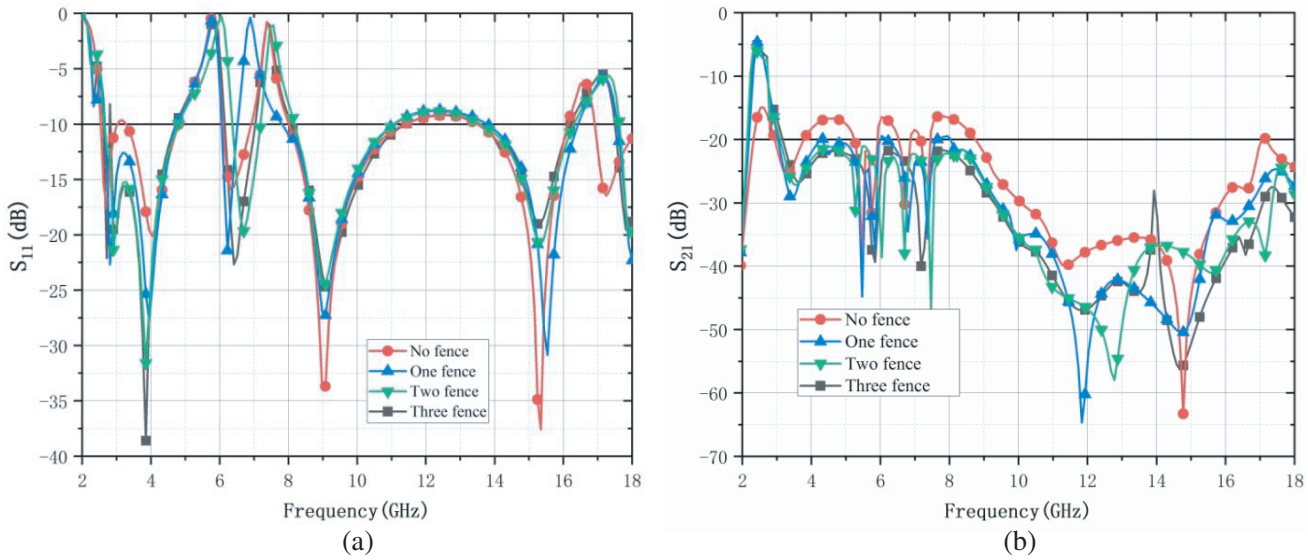

Figure 5. The S parameters of the four antennas. (a) S_{11}. (b) S_{21}.

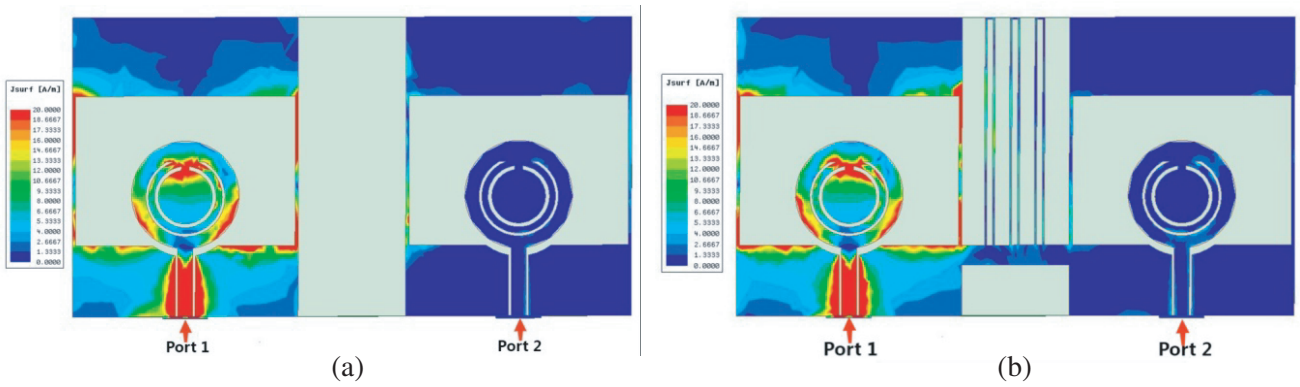

Figure 6. Simulated current distributions at different structures. (a) Antenna without isolation structures. (b) Antenna with isolation structures.

2.3. Isolation Structure Analysis

A fence-type isolation structure of the flexible MIMO antenna is studied. Three fence-type branches make up the isolation structure, and Figure 5 analyzes how the number of branches affects the S-parameters. By comparing the antenna's simulated S_{11} and S_{21} with and without various numbers of isolation branches, we can find that when two fence-type branches are added, S_{21} of the antenna is all below -20 dB in bands of 3.1–18 GHz, and S_{21} of the antenna tends to be stable with three fence-type branches. However, adding isolation branches broadens the antenna's bandwidth in the low-frequency part. Through careful consideration, the number of branches is 3. Figure 6 compares antenna current charts with isolated branches, which illustrate that the isolated branches can interrupt the current flow between two ports.

3. RESULTS AND DISCUSSIONS

3.1. S-Parameter

Figure 7 displays the antenna's simulated and actual S_{11} and S_{21} values. The measured operating bandwidth covers 3.0–15.7 GHz with blocking bands of 5.0–6.5 and 7.0–7.9 GHz, and the actual measurement S_{21} is less than -20 dB.

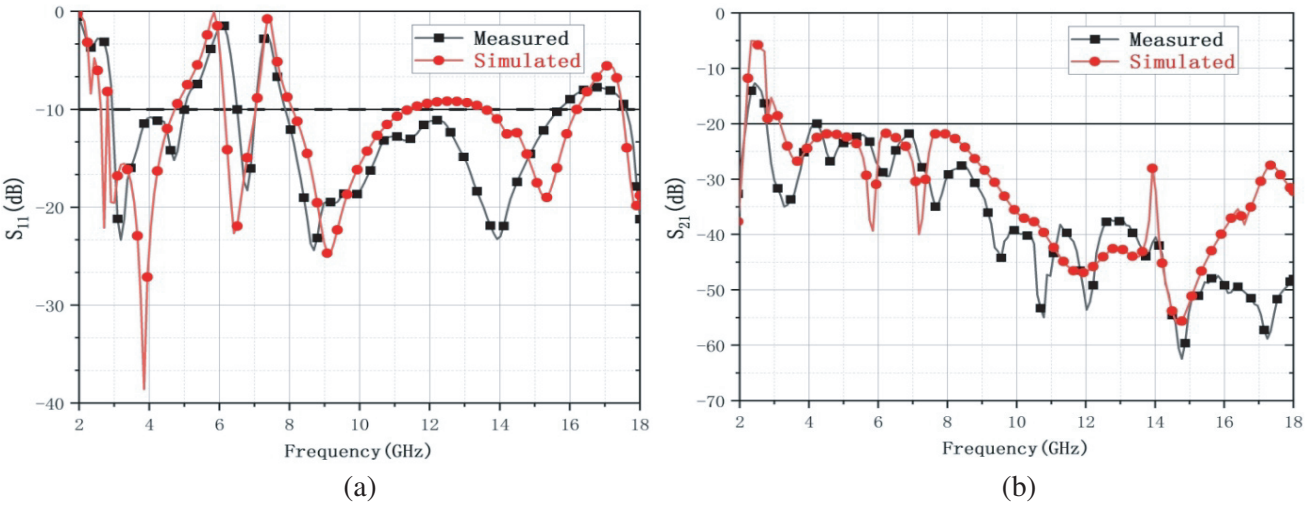

Figure 7. Measured and simulated S-parameters of antenna. (a) S_{11}. (b) S_{21}.

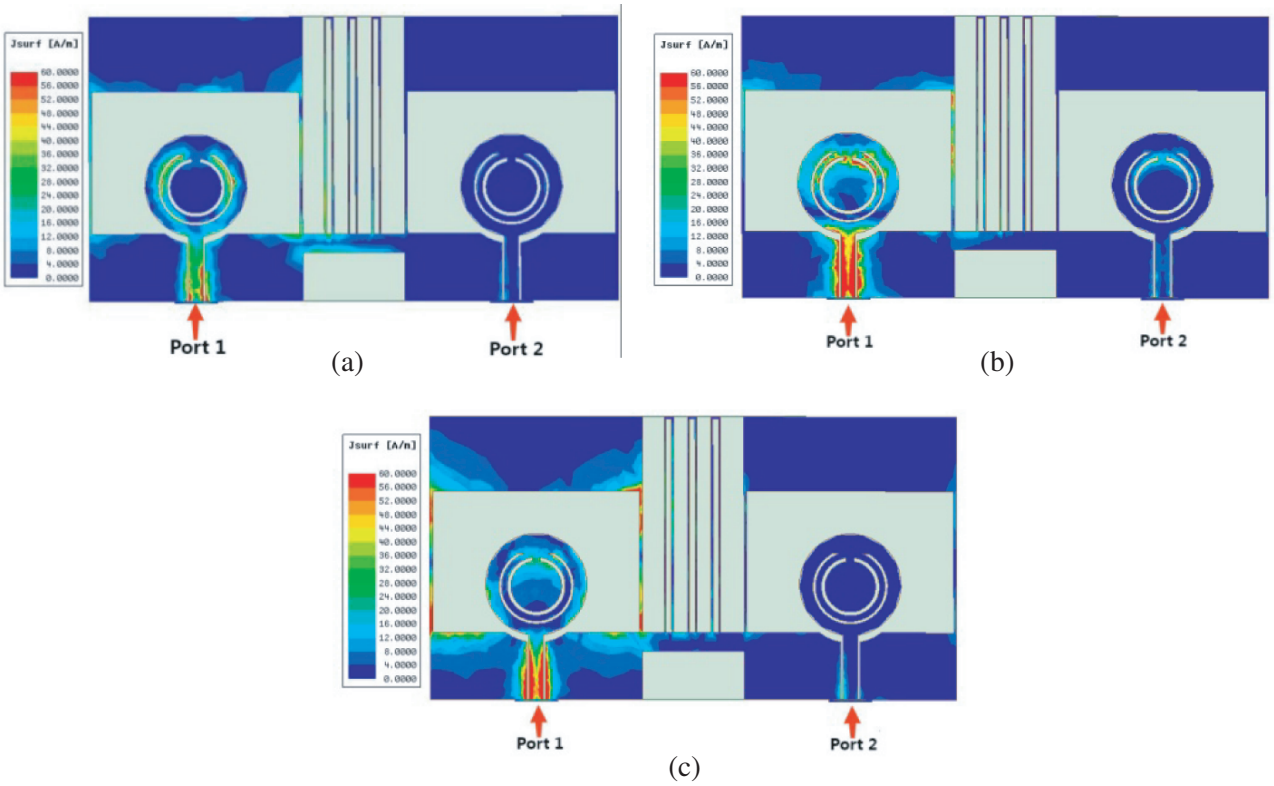

Figure 8. Simulated current distributions at (a) 5.4 GHz, (b) 7.4 GHz, (c) 9 GHz.

3.2. The Current Distribution

The current distributions at 5.4, 7.4, and 9 GHz are depicted in Figure 8, when a 50 load is supplied to port 2, and port 1 is excited to drive the antenna. In Figure 8(a), the current is mainly focused on the long C-shaped slot and the feed line at 5.4 GHz. In Figure 8(b), the current is mainly focused on the short C-shaped slot and the feed line at 7.4 GHz. In Figure 8(c), the current is mainly focused on the feeder line at 9 GHz.

3.3. Radiation Patterns

Figure 9 depicts simulated and actual radiation patterns of the antenna at 4, 6.5, and 10 GHz. Additionally, when port 2 is linked with a 50 Ω load and port 1 excited, the antenna is measured. The comparisons demonstrate that the H-plane's radiation patterns are roughly omnidirectional in both simulation and measurement. It displays consistent bidirectional (dumbbell-shaped) radiation performance on the E-plane at 4 and 6.5 GHz. The E-plane and H-plane radiation patterns present light distortion at 10 GHz. Overall, the introduced flexible antenna still has a good radiation performance in UWB.

3.4. Envelope Correlation Coefficient and Diversity Gain (DG)

Estimating the degree of correlation between components in a MIMO system requires knowledge of the quantity known as envelope correlation coefficient (ECC). Equation (2) can be used to calculate the

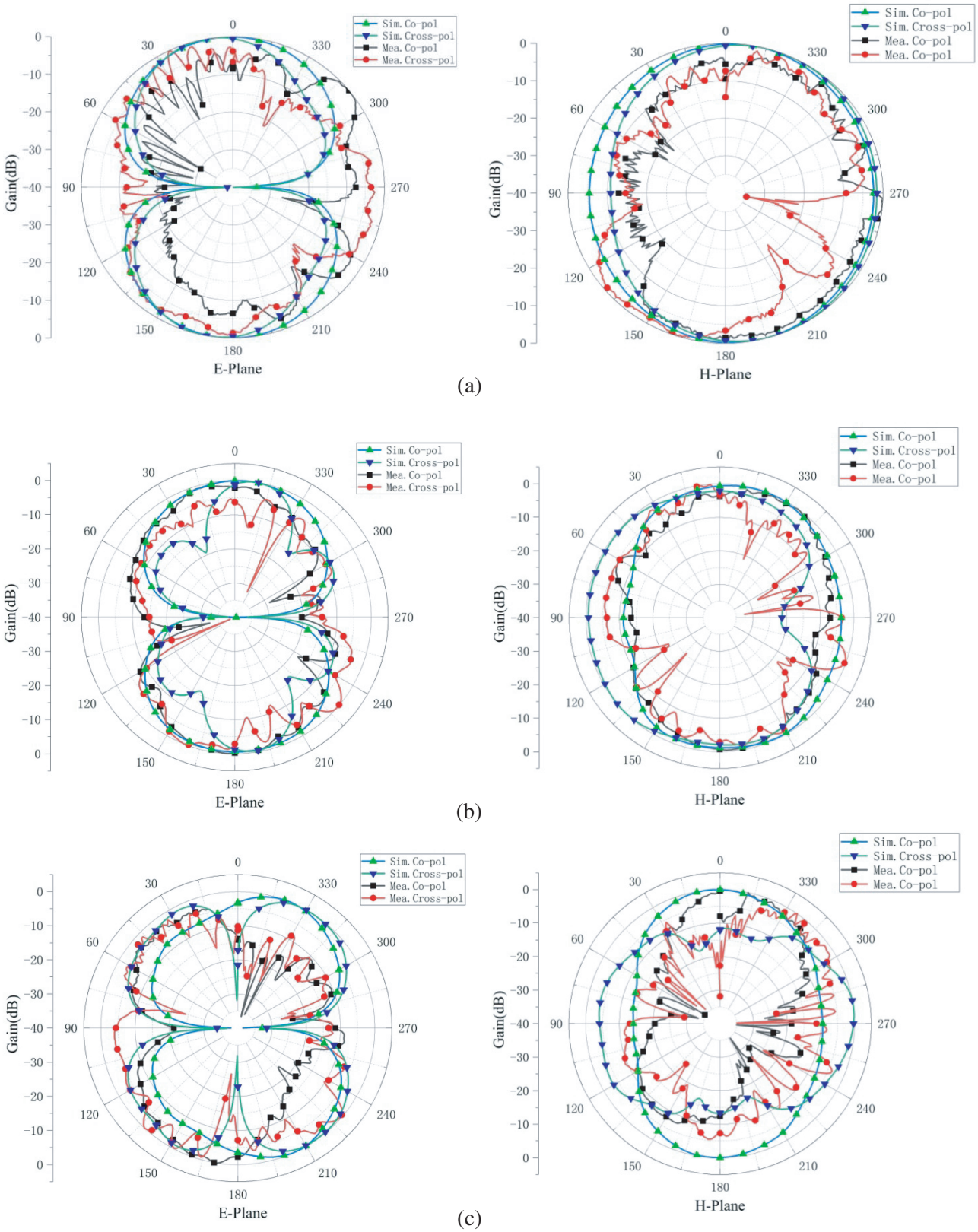

Figure 9. Simulated and measured antenna radiation patterns. (a) At 4 GHz. (b) At 6.5 GHz. (c) At 10 GHz.

ECC from the S-parameters.

$$\rho_e(i,j,N) = \left| \frac{\sum_{n=1}^{N} S_{i,n}^* S_{n,j}}{\left| \prod_{k=i,j} \left(1 - \sum_{n=1}^{N} S_{k,n}^* S_{n,k}\right) \right|^{1/2}} \right|^2 \tag{2}$$

The antenna must have relatively high efficiencies to maintain the validity of Equation (2) [15]. Based on antenna far-field measurement, the more accurate ECC values can be estimated using Equation (3).

$$\rho_e = \frac{\left| \iint \left[\vec{F}_1(\theta,\varphi) \times \vec{F}_2(\theta,\varphi) \right] \right| d\Omega^2}{\iint \left| \vec{F}_1(\theta,\varphi) \right|^2 d\Omega \iint \left| \vec{F}_2(\theta,\varphi) \right|^2 d\Omega} \tag{3}$$

Similarly, diversity gain (DG), which may be determined using the following Equation (4), is important when the properties of MIMO antennas are assessed.

$$\mathrm{DG} = 10\sqrt{1-(\mathrm{ECC})^2} \tag{4}$$

Figure 10(a) demonstrates that three type ECC values are all less than 0.005. Figure 10(b) shows three type DGs of the MIMO antenna are better than 9.998 within the operational band.

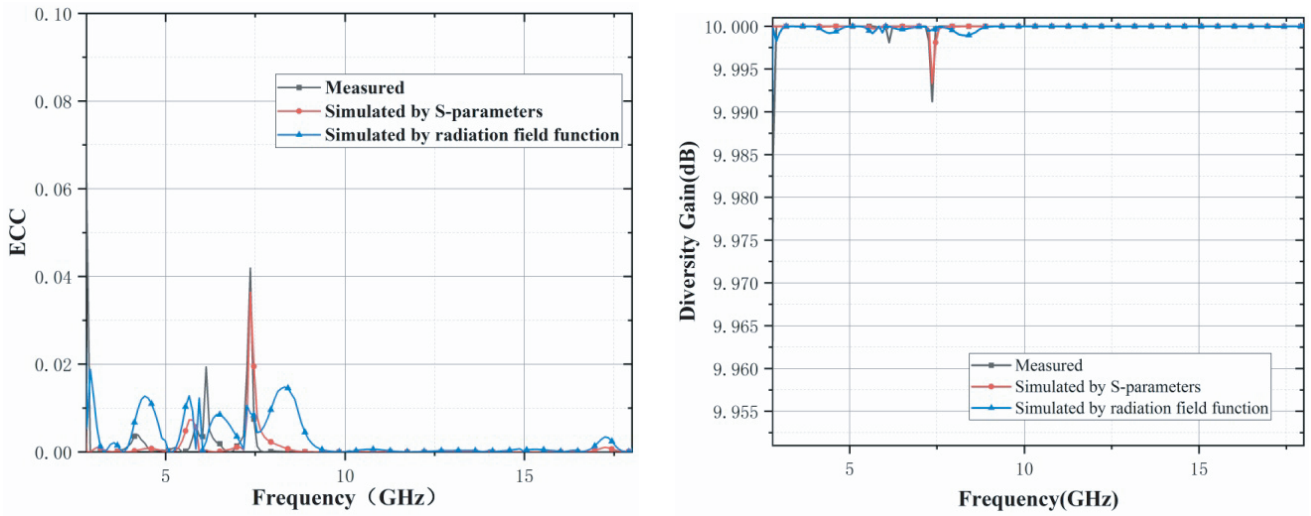

Figure 10. Results of ECC and DG simulations and measurements. (a) ECC. (b) DG.

3.5. Gain

The proposed antenna's peak gains are displayed in Figure 11. The measured gains change slightly under the influence of the test environment, and in the stopband, it is significantly decreased, demonstrating that the antenna is effective at preventing interference in the WLAN and X bands. The observed gain fluctuates between -2 and 6.2 dB.

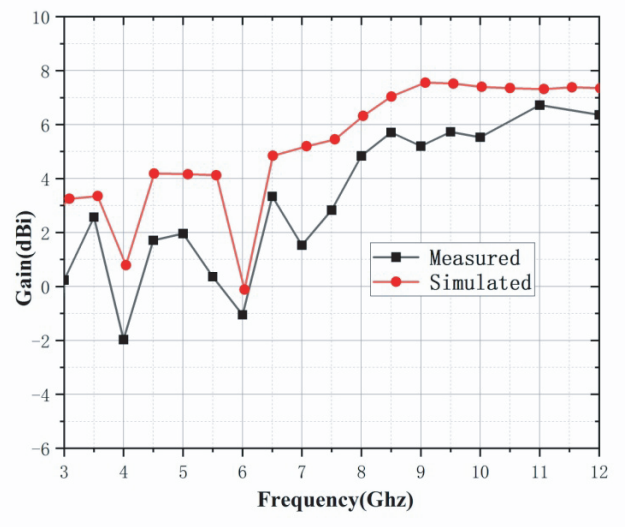

Figure 11. Peak gain of the present antenna.

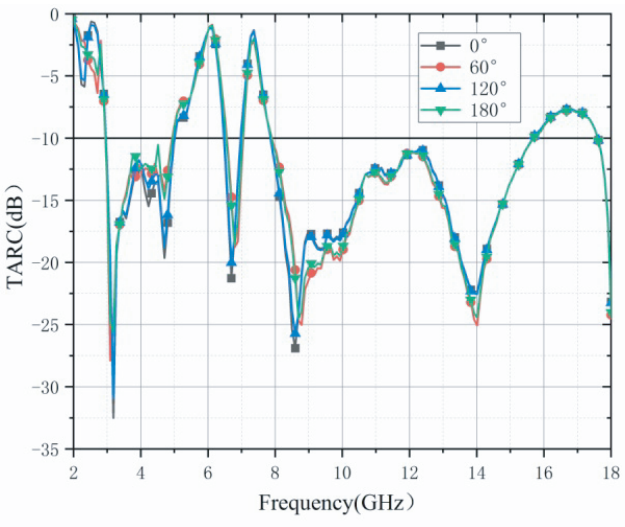

Figure 12. TARC of the proposed antenna.

3.6. Total Active Reflection Coefficient

The total active reflection coefficient (TARC) metric is used to assess the isolation between antenna parts. The TARC is expressed as follows when the input signal's phase (θ) is changed.

$$\text{TARC} = N^{-0.5}\sqrt{\sum_{i=1}^{N}\left|\sum_{k=1}^{N} S_{ik}e^{j\theta_{k-1}}\right|^2} \tag{5}$$

The TARC curves are seen in Figure 12. Figure 12 demonstrates how the observed value at 3.5–4.5 GHz changes when θ varies by 60 and 180. The measured results are below -10 dB over the whole experimental frequency range. TARC's bandwidth ensures high isolation among various ports in the MIMO antenna [16].

3.7. Flexibility Study

When a flexible MIMO antenna is integrated into a device, it is inevitable to bend and deform. Therefore, it is an important indicator to study whether the antenna can work adequately in the bending state. In Figure 13, the measured antenna is bent at the H-plane and E-plane. By bending the antenna to various degrees and measuring its S-parameters in the H-plane and E-plane, the soft properties of the antenna are seen. Figure 14 displays the antenna's measured S-parameters under bending conditions. The curves of S_{21} demonstrate that the planned antenna has acceptable isolation under two bending

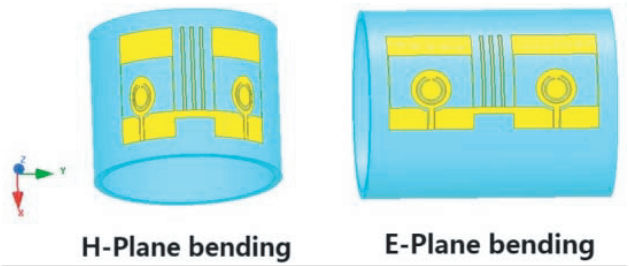

Figure 13. The measured antenna bending at H-plane and E-plane.

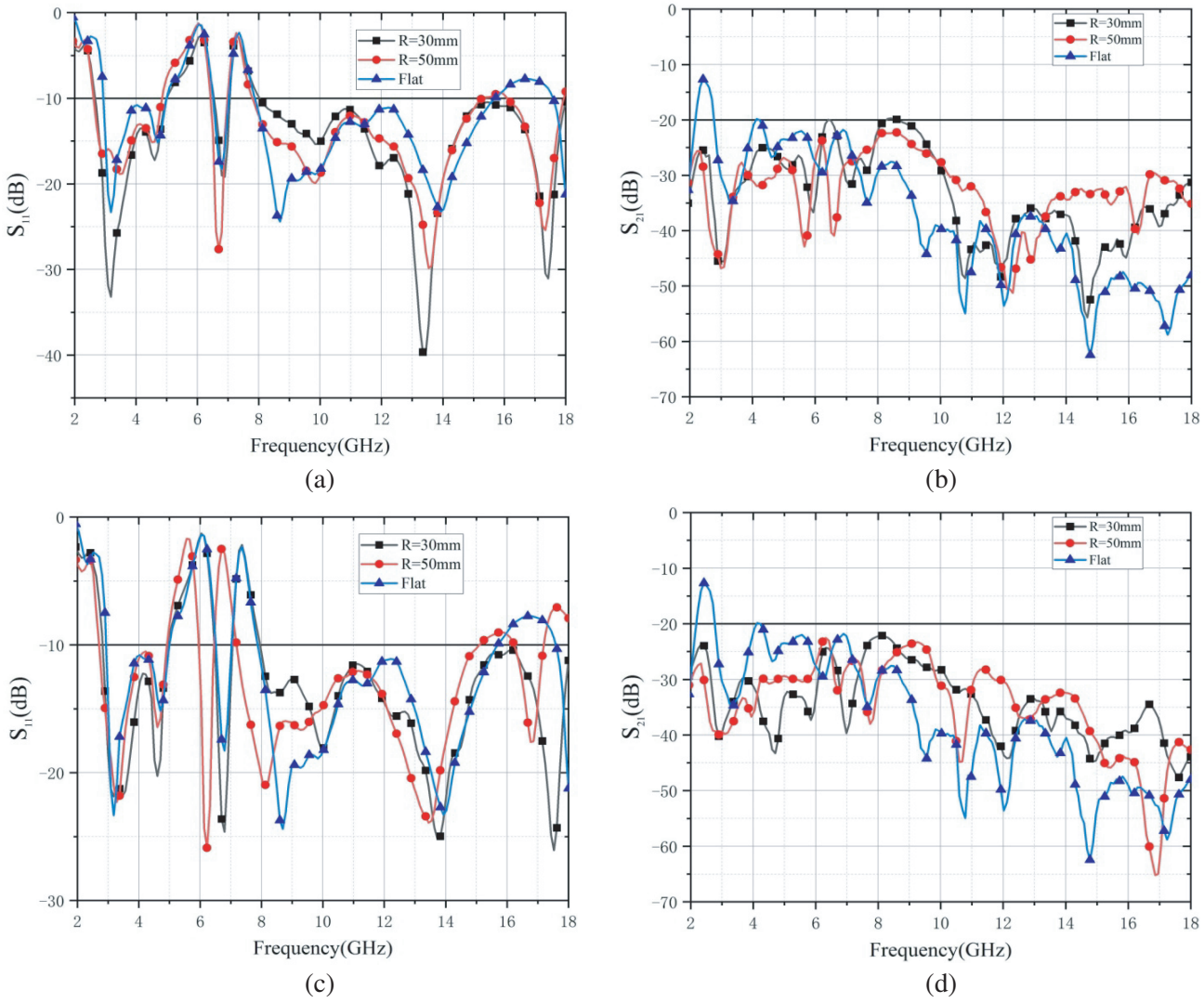

Figure 14. S-parameters in different conditions. (a) S_{11} on H-Plane. (b) S_{21} on H-Plane. (c) S_{11} on E-Plane. (d) S_{21} on E-Plane.

situations when the antenna is rotated along the H and E planes. However, if the antenna is curved in the direction of the E-plane, S_{11} would be visibly affected.

3.8. The Effects of the Human Body

For investigating the flexible MIMO antenna's wearable performances, the influence of the antenna on the body can be tested by placing it on the back, arms, and thighs. The S-parameter measurement results are depicted in Figure 15. The operating bandwidths of both the low-frequency and high-frequency components become narrow when the antenna is mounted on the back. The high-frequency operating bandwidth is more compromised when the antenna is mounted on the thigh, but the operational criteria are still met. Additionally, the S_{21} curve demonstrates that the antenna's isolation is less than -20 dB. The measured S-parameters of the bending antenna on the body differ mildly from those on flat plane, although both fulfill the design specifications.

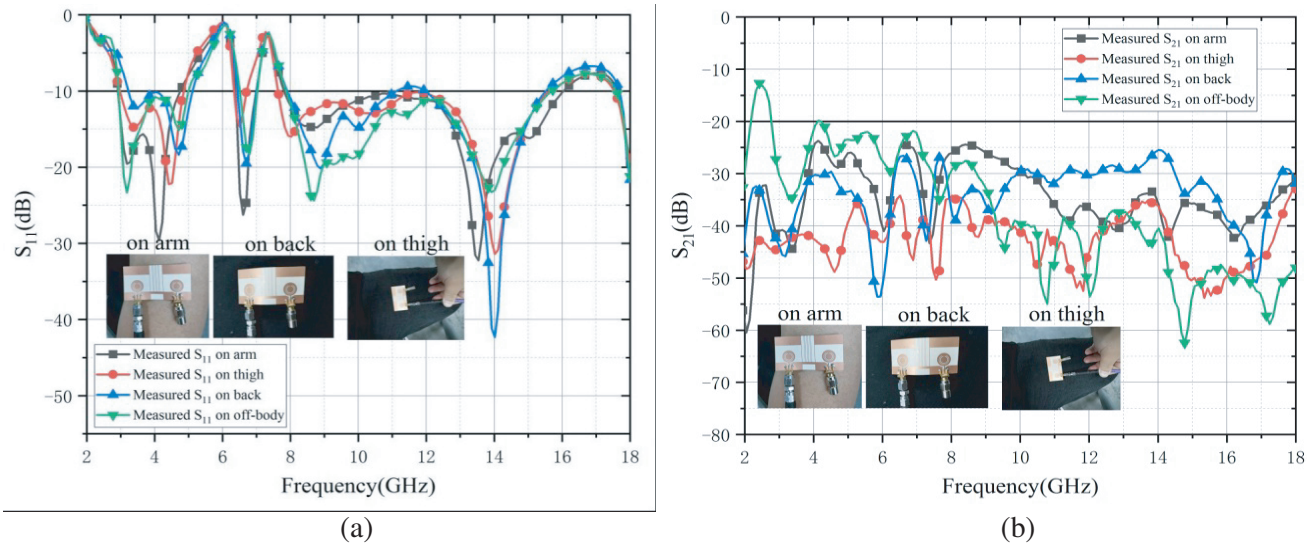

Figure 15. S-parameter measurements for the proposed antenna applied to human tissue. (a) S_{11}. (b) S_{21}.

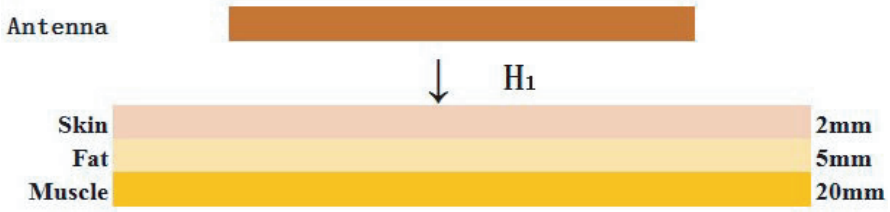

Figure 16. A simulation of the antenna moving toward the human body.

3.9. Specific Absorption Rate Evaluation

Specific absorption ratio (SAR) is the impact of radiated energy on human tissue when a flexible antenna is used [17]. The following is the formula used to calculate the local SAR value:

$$\mathrm{SAR} = \frac{\sigma E^2}{\rho} \tag{6}$$

σ stands for electrical conductivity, E for the root mean square of square value of electric field intensity, and ρ for the density of human tissue.

In Figure 16, SAR values are estimated by mounting the antenna on a three-layer human tissue model, which is made up of a 20 mm layer of muscle with $\varepsilon_r = 52.67$, $\sigma = 1.77$ [S/m], a 5 mm layer of fat with $\varepsilon_r = 5.27$, $\sigma = 0.11$ [S/m], and a 2 mm layer of skin with $\varepsilon_r = 37.95$, $\sigma = 1.49$ [S/m]. The model size is $40 \times 66.5 \times 40\,\mathrm{mm}^3$ in the HFSS simulation.

The highest SAR values derived from HFSS simulations are displayed in Table 2. The input power is 0.1 W, and the antenna's distance from the human tissue is 5 mm. The data in Table 2 fall below the EU threshold of 2 W/kg/10 g. The SAR distribution with an H1 of 5 mm is shown in Figure 17.

Table 2. SAR maximum values at various frequencies.

Frequency (GHz)	4 GHz	9 GHz	11 GHz
10 g Tissue (W/kg)	1.49	1.48	0.38

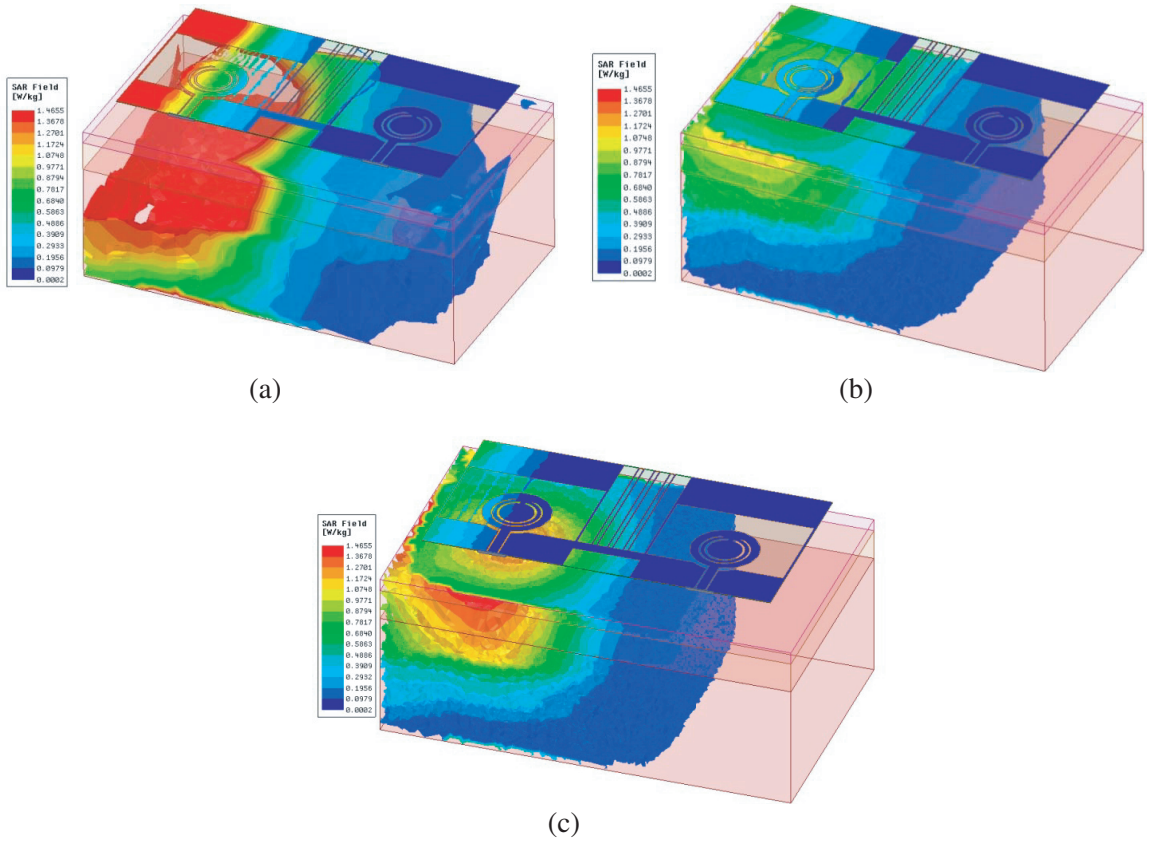

Figure 17. SAR distribution simulation in a 10 g model of human tissues. (a) 4 GHz, (b) 9 GHz and (c) 11 GHz.

Table 3. Comparison of some proposed UWB MIMO antennas.

Ref.	**Sub**	Bandwidth (GHz)	Port number	Notches	Connected ground	Isolation (dB)	ECC	DG	Feeder method
[5]	FR4	2–14	2	1	Yes	< -30	NA	NA	Microstrip
[6]	FR4	3.0–10.7	2	4	Yes	< -25	0.01	10	Microstrip
[7]	FR4	3.01–12.5	4	2	No	< -20	0.05	NA	CPW
[8]	Kapton Polyimide	3.2–13	2	0	No	< -23	0.01	9.98	CPW
[9]	Silicone rubber	3.1–12	4	0	Yes	< -20	0.1	9.4	Microstrip
[11]	Jeans cloth	1.83–13.82	2	0	Yes	< -21	0.059	9.9	Microstrip
[12]	Cotton	2.26–20	2	0	Yes	< -20.6	0.001	NA	Microstrip
[13]	LCP	2.4–11.3	2	1	No	< -23	0.008	9.99	CPW
This work	LCP	3.0–15.7	2	2	Yes	< -20	0.045	9.998	CPW

3.10. Performance Comparison

The substrate, operational bandwidth, stopband range, isolation, and ECC of the developed antenna are compared to those of UWB-MIMO antennas recently suggested in the literature. Table 3 presents the comparing results. The antennas mentioned in the literature [5–7] are non-flexible UWB MIMO antennas. The UWB MIMO antennas based on flexible dielectric substrates are used in all of the antennas in the literature [8, 9, 11–13]. The flexible MIMO antenna with two notched bands has wider bandwidth, high isolation, and CPW feeder by comparison.

4. CONCLUSION

In this paper, a flexible dual-band notched UWB-MIMO slot antenna on an LCP substrate is suggested. Fence-like branches have been added for high isolation, and the measured port isolation is better than 20 dB with UWB coverage (3.0–15.7 GHz). The notched bands of the antenna are achieved by etching slots, which can block the interference signals of WLAN and X-band systems. The measured flexible UWB-MIMO antenna exhibits extremely good characteristics with regard to ECC (< 0.01), DG (> 9.99), and TARC (< -10 dB). Additionally, the antenna performs well on human tissues. As a result, the flexible UWB MIMO antenna is suitable for many wearable IoT applications.

REFERENCES

1. FCC, "First report and order," FCC: First report and order on ultra-wideband technology, 2002, Washington, DC, USA, 2022.
2. See, T. S. P., A. M. L. Swee, and Z. N. Chen, "Correlation analysis of UWB MIMO antenna system configurations," *2008 IEEE International Conference on Ultra-Wideband*, Sept. 2008.
3. Jusoh, M., M. F. B. Jamlos, M. R. Kamarudin, and M. F. B. Abd Malek, "A MIMO antenna design challenges for UWB application," *Progress In Electromagnetics Research B*, Vol. 36, 357–371, 2012.
4. Saritha, V. and C. Chandrasekhar, "A study and review on frequency band notch characteristics in reconfigurable MIMO-UWB antennas," *Wireless Personal Communications*, Vol. 118, No. 4, 2631–2661, Feb. 14, 2021.
5. Tripathi, S., A. Mohan, and S. Yadav, "Performance study of a fractal UWB MIMO antenna for on-body WBAN applications," *Analog Integrated Circuits and Signal Processing*, Vol. 95, No. 2, 249–258, Feb. 28, 2018.
6. Modak, S. and T. Khan, "A slotted UWB-MIMO antenna with quadruple band-notch characteristics using mushroom EBG structure," *AEU — International Journal of Electronics and Communications*, Vol. 134, 153673, May 2021.
7. Srivastava, K., A. Kumar, B. K. Kanaujia, S. Dwari, and S. Kumar, "A CPW-fed UWB MIMO antenna with integrated GSM band and dual band notches," *International Journal of RF and Microwave Computer-Aided Engineering*, Vol. 29, No. 1, e21433, Oct. 10, 2018.
8. Raad, H. K., "An UWB antenna array for flexible IoT wireless systems," *Progress In Electromagnetics Research*, Vol. 162, 109–121, 2018.
9. Govindan, T., S. K. Palaniswamy, M. Kanagasabai, S. Kumar, T.Rama Rao, and M. G. N. Alsath, "Conformal quad-port UWB MIMO antenna for body-worn applications," *International Journal of Antennas and Propagation*, Vol. 2021, 1–13, Dec. 30, 2021.
10. Zhou, X., T. Leng, K. Pan, M. Abdalla, K. S. Novoselov, and Z. Hu, "Conformal screen printed graphene 4×4 wideband MIMO antenna on flexible substrate for 5G communication and IoT applications," *2D Materials*, Vol. 8, No. 4, 045021, Aug. 20, 2021.
11. Dey, A. B., S. S. Pattanayak, D. Mitra, and W. Arif, "Investigation and design of enhanced decoupled UWB MIMO antenna for wearable applications," *Microwave and Optical Technology Letters*, Vol. 63, No. 3, 845–861, Nov. 10, 2020.
12. Jayant, S., G. Srivastava, and R. Purwar, "Bending and SAR analysis on UWB wearable MIMO antenna for on-arm WBAN applications," *Frequenz*, Vol. 75, No. 5–6, 177–189, Mar. 1, 2021.

13. Du, C. and G. Jin, "A compact CPW-fed band-notched UWB-MIMO flexible antenna for WBAN application," *Journal of Electromagnetic Waves and Applications*, Vol. 35, No. 8, 1046–1058, 2021.
14. Du, C., Z. Yang, and S. Zhong, "A compact coplanar waveguide-fed band-notched four-port flexible ultra-wide band-multi-input-multi-output slot antenna for wireless body area network and Internet of Things applications," *International Journal of RF and Microwave Computer-Aided Engineering*, Vol. 32, No. 9, e23289, 2022.
15. Kulkarni, J., A. Desai, C.-Y. D. Sim, "Wideband four-port MIMO antenna array with high isolation for future wireless systems," *AEU — International Journal of Electronics and Communications*, Vol. 128, Jan. 1, 153507, 2021, accessed 26 Feb. 2021.
16. Desai, A., M. Palandoken, I. Elfergani, I. Akdag, C. Zebiri, J. Bastos, J. Rodriguez, and R. A. Abd-Alhameed, "Transparent 2-element 5G MIMO antenna for sub-6 GHz applications," *Electronics*, Vol. 11, No. 2, 251, 2022.
17. Li, Y. J., Z. Y. Lu, and L. S. Yang, "CPW-fed slot antenna for medical wearable applications," *IEEE Access*, Vol. 7, 42107–42112, 2019.